Chemical Science

ROYAL SOCIETY OF CHEMISTRY

EDGE ARTICLE

View Article Online
View Journal | View Issue

Cite this: *Chem. Sci.*, 2024, **15**, 2586

All publication charges for this article have been paid for by the Royal Society of Chemistry

Received 14th December 2023
Accepted 7th January 2024

DOI: 10.1039/d3sc06719j

rsc.li/chemical-science

Leveraging metal node-linker self-assembly to access functional anisotropy of zirconium-based MOF-on-MOF epitaxial heterostructure thin films†

Suvendu Panda, Susmita Kundu, Pratibha Malik and Ritesh Haldar *

Chemically robust, functional porous materials are imperative for designing novel membranes for chemical separation and heterogeneous catalysts. Among the array of potential materials, zirconium (Zr)-based metal–organic frameworks (MOFs) have garnered considerable attention, and have been investigated for applications related to gas separation and storage, and catalysis. However, a significant challenge with Zr-MOFs lies in their processibility, particularly in achieving homogenous thin films and controlling functional anisotropy. The recent developments in MOF thin film fabrication methodologies do not yield a solution to achieve mild reaction condition growth of Zr-MOF thin films with epitaxial MOF-on-MOF geometry (*i.e.* functional anisotropy). In the current work, we have devised a straightforward methodology under room temperature conditions, which enables epitaxial, oriented MOF-on-MOF thin film growth. This achievement is accomplished through a stepwise self-assembly approach involving Zr nodes and linkers on a functionalized substrate. This *de novo* developed strategy of functionality design is demonstrated for UiO-66 (University of Oslo) type Zr-MOFs. We have demonstrated the precise placement of chemical functionalities within the thin film structure, allowing for controlled chemical diffusion and regulation of diffusion selectivity.

Introduction

Metal–organic frameworks (MOFs) have garnered considerable interest as synthetic porous materials with potential utility in chemical separation and catalysis.[1–5] This is because a combination of inorganic (metal and metal-oxo cluster) and organic (functionalized with metal coordinating groups) components in MOFs offers a high degree of structural order, very high permanent porosity, large chemical space, topological diversity, and structure predictability.[1,6–8] These features have been well-explored in the past for the aforementioned applications and beyond, such as light harvesting,[9] sensing,[10,11] and optoelectronics.[12] It is realized that for real-time applications (*e.g.* membranes for gas and ion separation, electrode materials, and electronics),[13–17] stability, processibility and functional complexity of the MOFs are necessary. Stability refers to thermal, hydrolytic, and wide pH range; processibility insinuates the fabrication of large area thin films, and functional complexity means the spatial control over the functionality (porosity and polarity).[18–20] In the context of stability, the use of higher oxidation states of metals (Zr^{4+}, Al^{3+}, and Cr^{4+}) has been a successful strategy.[21–24] In particular, Zr^{4+}-based MOFs show exceptional stability[22,25] under high temperature, pressure, and pH conditions, and as a result, have been well-explored in heterogeneous catalysis and adsorption-based chemical separation.[22] There are relatively few reported membrane-based separation applications for these Zr^{4+}-based MOFs, mainly due to the absence of suitable thin film fabrication methodologies.[26–29] Furthermore, the realization of the intricate functional structure of a Zr-MOF, *i.e.* in the form of a MOF-on-MOF[17] heterostructure thin film is unprecedented. It is important to highlight that the MOF-on-MOF structure encompasses core–shell, yolk–shell and film-on-film geometry.[30,31] These heterostructures have been created using MOFs of varying topologies and compositions. Comparative analysis with the original MOFs has demonstrated improved adsorption, diffusion and catalytic properties in these heterostructures.[32–34]

One straightforward method of fabricating a MOF thin film is by the conventional solvothermal (one-pot mixing of the metal and linker) method,[35–38] in which the crystals grow on a solid support during the crystal growth process in a solution. In this method, control over the deposition rate, homogeneity of the thin film and crystal orientation is difficult. Improved methodologies have been developed in recent years;[39] these are layer-by-layer liquid-phase epitaxy,[40,41] chemical vapor deposition,[42,43] (solution) atomic layer deposition,[44,45] electrodeposition,[46,47] and vapor-assisted conversion.[48] In these methods, the metal–linker reaction conditions are fine-tuned (by using the solid-support surface functionality, concentration, solvent, temperature, or coordination modulation approach) to achieve controlled growth of the crystalline film. Some of these methods have been applied to Zr^{4+}-based MOFs also,

Tata Institute of Fundamental Research Hyderabad, Gopanpally, 500046 Hyderabad, India. E-mail: riteshhaldar@tifrh.res.in

† Electronic supplementary information (ESI) available. See DOI: https://doi.org/10.1039/d3sc06719j

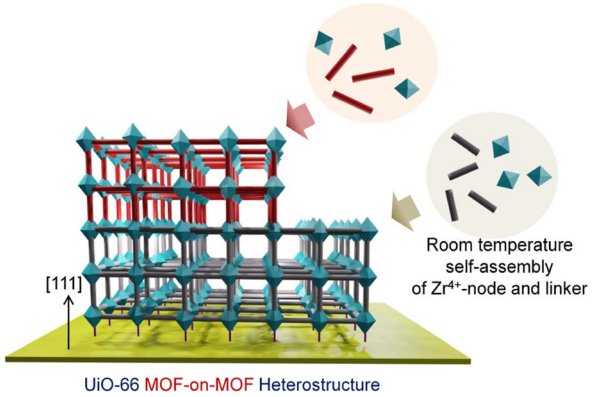

Scheme 1 Schematic illustration of UiO-66 MOF-on-MOF epitaxial, oriented heterostructure formation, using a room temperature self-assembly approach (solid bars = linkers and octahedron = Zr^{4+} node).

particularly for UiO types (University of Oslo).[49] We have realized that none of these methodologies are under ambient conditions and allow spatial control over the MOF functionality, *i.e.* a crystalline, oriented MOF-on-MOF heterostructure[50,51] (see Table S1†). This is mainly because of the Zr^{4+}-coordination chemistry: (a) Zr–O cluster (acting as a node) formation requires high temperature and (b) at higher temperature, MOF-on-MOF heterostructure formation is challenging because of the reversible nature of coordination bonds. Development of such a thin film fabrication methodology for highly robust Zr^{4+}-based MOFs has substantial advantages; (i) MOF-on-MOF heterostructures can be made for device-based applications (membranes, rectifiers and sensors),[50,52–54] (ii) easy fabrication of large-area membranes having preferred orientation of the nanochannels,[55] and (iii) easy incorporation of temperature sensitive chemical components, *e.g.* metal catalysts. In the current work, we have formulated a simple strategy to realize Zr^{4+}-based MOF thin films under room temperature conditions, which also allow the fabrication of a MOF-on-MOF heterostructure having a high crystalline orientation (Scheme 1). This is exemplified using a prototype UiO-66 MOF with various linker functionalities[56] (1,4-benzene dicarboxylic acid, bdc; 2-amino-1,4-benzenedicarboxylic, bdc-NH_2; 2,6-dibromo-1,4-benzenedicarboxylic acid, bdc-Br_2). It is revealed that under ambient conditions the chosen precursors and reaction parameters allow fast self-assembly and nucleation with a preferred crystalline orientation. The oriented MOF thin films also exhibited high optical transparency and fast adsorption of water and methanol vapours, confirming their porosity. Chemical isomer diffusion studies on the functionally complex MOF-on-MOF heterostructure of the UiO-66 thin films unveiled that the spatial distribution of the functionalities (porosity and functional groups) is precise and can be utilized further to improve diffusion selectivity.

Results and discussion

Ambient condition synthesis of oriented UiO-66 MOF thin films

An UiO-66 MOF is constructed by linking a Zr_6O_8 node with a bdc linker. The node or secondary building unit (SBU), formed *in situ*, is kinetically and thermodynamically robust resulting in a highly stable framework structure. The cross-linking of the node and linker yields two distinct interconnected cages of dimensions 8 and 11 Å. Access to these cages is possible *via* a window with a dimension of ~6 Å. The reported oriented thin films of UiO-66 indicate that the preferential crystal growth orientation is along [111] (Fig. 1a). Changing the surface functionality does not alter the preference. This preference is due to the high density of the Zr–O node on the crystallographic (111) plane (Fig. S1†). To measure the extent of orientation preference, the intensity ratio of diffraction peaks related to the (111) and (200) planes is compared. Note that keeping the [111] growth orientation does not expose the pore windows to the surface (Fig. S1†), but preferential growth allows better interconnection of the pore windows. This will allow faster diffusion of molecules, which is important for molecular separation and catalysis.[27]

Previously, it was revealed that using a vapor-assisted conversion method (at >373 K) is feasible to make an oriented monolithic thin film of Zr-MOFs.[48] Following a similar methodology, it was not achievable under our experimental lab

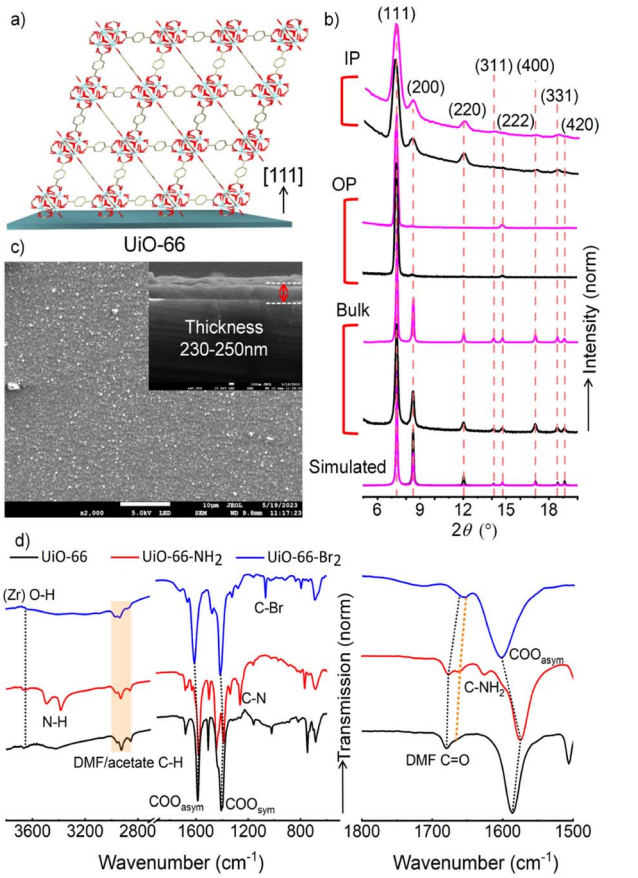

Fig. 1 (a) [111] oriented UiO-66 MOF, (b) comparison of out and in-plane XRD patterns of the UiO-66 (black) and UiO-66-NH_2 (pink) thin films with the simulated and as-synthesized powder XRD patterns, (IP = in-plane and OP = out-of-plane), (c) SEM morphology (scale bar = 10 μm) and cross-section (inset) of the UiO-66 thin film, and (d) (left) IRRAS of UiO-66, UiO-66-NH_2, and UiO-66-Br_2; (right) zoomed in 1800–1500 cm^{-1}; dotted lines are a guide to the eyes.

conditions (issues with crystallinity and homogeneity, see Fig. S2†). We have realized that subtle factors, such as vapor pressure, humidity and chemical purity can be limiting parameters. In other reports by Wöll and coworkers,[57] and Fischer and coworkers,[58] the layer-by-layer approach of Zr-node and linker assembly to make UiO-66-NH_2 was carried out at elevated temperature (343 K), and the resultant thin film did not exhibit a preferred crystalline orientation. UiO-66 was also deposited by the electrochemical deposition method but did not exhibit a crystalline orientation.[46] More recently a new approach of making the UiO-66 thin film under ambient conditions was successful by using a seed assisted coating process.[28] In this method, a thin film with a crystallographic preferred orientation (CPO) of 7.9 ((111)/(002)) could be prepared by spin coating the precursor solutions on the seeded substrate (reported methods in Table S1†). To achieve the preferential orientation under ambient conditions, we have chosen known precursors which can allow MOF crystallization under ambient conditions. Recent studies indicated that the node, $Zr_6O_4(OH)_4(OMc)_{12}$, synthesized using a coordination modulator methacrylic acid, can be assembled with a dicarboxylate linker to achieve UiO-66 MOF under ambient conditions.[59] In our modified synthesis approach, the precursors are $(Zr_6(\mu_3\text{-}O)_4(\mu_3\text{-}OH)_4(OOCCH_3)_{12})$ metal cluster solution and 1,4-benzene dicarboxylic acid (bdc) dissolved in DMF (Experimental section). These precursors are mixed in a ratio of 2 : 1 (stock solution v/v), and drop cast on a –OH functionalized Si/SiO_2 (1 cm × 1 cm) substrate at 298 ± 5 K and a humidity of 50–70%. We have observed that within 2 h the surface is partially covered with deposition of MOF crystals. A repetition of the same process yielded a homogeneously covered UiO-66 thin film, as confirmed by X-ray diffraction (XRD) experiments and scanning electron microscopy (SEM) images (Fig. 1b and c). The orientation of the thin film is confirmed using out and in-plane XRD techniques. In comparison to the simulated and as-synthesized powder (at 298 ± 5 K and a humidity of 50–70%) XRD patterns, the out-of-plane XRD pattern of the thin film exhibited substantially reduced diffraction peak intensity corresponding to the (200) plane. This resulted in an unprecedented CPO value of 16, for (111)/(200). The in-plane XRD pattern showed diffraction peaks related to the (111), (200), (220), (400), and (331) planes, suggesting a [111] oriented UiO-66 thin film. The SEM images in Fig. 1c confirmed the homogeneity of the thin film.

To realize homogenous thin film formation, we have optimized the following parameters: precursor concentration and volume and duration of self-assembly (see Tables S2–S4 and Fig. S3–S15†). (A) Initially, we drop cast 50 μL of a 1 : 1 (stock solution v/v) mixture of metal cluster solution and bdc solution (7.184 mM) on a –OH functionalized Si/SiO_2 (1 cm × 1 cm) substrate. This led to the rapid formation of white UiO-66 crystals within 30 minutes. Upon thorough washing with DMF, we have observed that the surface coverage was incomplete (Fig. S16a†). We realized that the precursor volume and ratio were not optimal. (B) Next, we increased the volume to 100 μL and the precursor ratio to 2 : 1 (stock solution v/v). This change resulted in slower crystallization, and we observed improved surface coverage after 2 h (Fig. S16b†). To achieve complete surface coverage, (C) we extended the reaction time to 3.5 and 5 h and observed that an extended duration of self-assembly lead to excess deposition, resulting in a roughened surface (Fig. S16c and d†). (D) Following these observations, we have repeated method B, and realized that two-times drop casting results in a uniformly covered and highly oriented thin film (Fig. 1b and c) (for details see the Experimental section). Note that the duration of the self-assembly does not change the size of the crystalline domains, as can be seen from a time-dependent full width at half maximum of the out-of-plane XRD peak corresponding to the (111) plane (Fig. S17a†). Nevertheless, a constant increase in peak intensity indicates the formation of new crystallites, which fill in the substrate surface yielding a homogeneous thin film (Fig. S17b†). Using a similar methodology, we could synthesize the UiO-66-NH_2 and UiO-66-Br_2 thin films, in which the linkers are NH_2-bdc and Br_2-bdc, respectively. For these two, the CPO (111)/(200) values calculated from the out-of-plane XRD patterns are ∼15 and ∼2.9, respectively, indicating a preferential growth direction of [111] (Fig. 1b and S18†). The SEM and atomic force microscopy images also confirm the homogeneity of the thin films (Fig. S19 and 20†).

After confirming oriented homogenous film formation, we have characterized the thin films using infra-red reflection absorption spectroscopy (IRRAS) to assess the chemical functionalities (Fig. 1d). For UiO-66, the characteristic asymmetric and symmetric COO stretching frequencies are observed at 1585 and 1390 cm^{-1}, respectively.[60,61] For UiO-66-NH_2 and UiO-66-Br_2 these frequencies are slightly shifted; they are 1575 and 1606 cm^{-1} (asymmetric) and 1386 and 1407 cm^{-1} (symmetric), respectively. These peak shifts are attributed to the basicity of $–COO^-$, which is modulated by the substitution of bdc. For the NH_2 substitution, basicity of $–COO^-$ is increased. This increases Zr^{4+}–O bond strength, and C–O bond strength is reduced. Hence $–COO^-$ stretching frequencies are shifted to a lower wavenumber. For Br-substitution, basicity of $–COO^-$ is reduced, and hence, $–COO^-$ stretching frequencies are shifted to a higher wavenumber. The characteristic $–NH_2$ (3495 and 3382 cm^{-1} are the asymmetric and symmetric stretching of the NH_2, respectively, 1625 cm^{-1} NH_2 bending) and C–Br (1061 cm^{-1}) vibrations in UiO-66-NH_2 and UiO-66-Br_2 (respectively) are distinct in the IRRAS spectra.[62] In addition to these, (Zr)O–H stretching (3660 cm^{-1}) from the node, C–H stretching from the acetate and DMF (2965–2852 cm^{-1}, orange shaded region), and C═O stretching of the adsorbed DMF are evident from the IRRAS spectra. The orange dotted line shows the evidence of C═O stretching from the acetates (precursor node solution, see Fig. S22†) or partially coordinated bdc/NH_2-bdc/Br_2-bdc linkers, indicating the inherent defects in UiO-66 MOFs.[59] The chemical and thermal stability (exposed to a halogenated solvent dichloromethane, followed by acetone and then heating at 393 K) of UiO-66, UiO-66-NH_2 and UiO-66-Br_2 (grown on Au) were confirmed by unaltered XRD patterns and IRRAS spectra (Fig. S21 and 23†).

After establishing the oriented film growth under ambient conditions, we have tested the feasibility of MOF-on-MOF heterostructure growth. Prior to this discussion, it is worth mentioning that the synthesized thin films maintain high

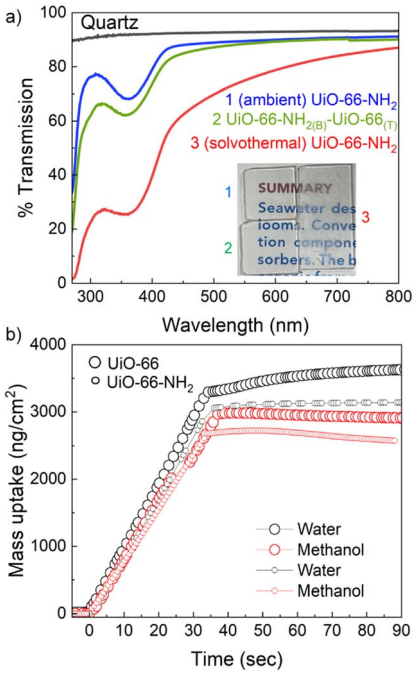

Fig. 2 (a) Transmission spectra (at 298 K) of bare quartz, the UiO-66-NH_2 thin films synthesized under the new ambient conditions and by the solvothermal method and UiO-66-$NH_{2(B)}$-UiO-$66_{(T)}$ grown on quartz substrates, inset: optical images of the thin films; (b) water and methanol vapour uptake profiles of the UiO-66 and UiO-66-NH_2 thin films at 298 K.

optical quality and mass diffusion (Fig. 2). High optical quality or light transmission features of the thin film can be important for optical (electronic) applications.[63] Mass diffusion is a key parameter for gas separation and catalysis applications.[64] The transmission spectra recorded for UiO-66-NH_2 and a MOF-on-MOF heterostructure of UiO-66-$NH_{2(B)}$-UiO-$66_{(T)}$ (B = bottom layer and T = top layer) grown on quartz substrates (*vide infra*) exhibit much reduced scattering in the visible range of the absorption spectrum compared to that of a solvothermally deposited UiO-66-NH_2 thin film (Fig. 2a). This feature, attributed to the lower roughness of the films, can allow better light penetration to the material. To measure the pore accessibility of the thin films, UiO-66 and UiO-66-NH_2 thin films are grown on self-assembled monolayer modified Au-coated quartz crystal sensors. These oriented thin films are mounted in a fluidic cell and tested for water and methanol vapour uptake (at 298 K) using a quartz crystal microbalance (QCM; see the Experimental section for the details of mass calculation using the Sauerbrey equation).[65] The mass uptake rate profiles indicated fast diffusion with water/methanol adsorption selectivities (*i.e.* mass uptake ratio at saturation) of 1.3 and 1.2 for UiO-66 and UiO-66-NH_2, respectively (Fig. 2b; for UiO-66-Br_2 see Fig. S27†). The preference for water adsorption is based on the smaller kinetic diameter of water compared to that of methanol,[66] (for UiO-66 and UiO-66-NH_2) thus confirming the diffusion into the pores of the MOF thin films.

MOF-on-MOF heterostructure

To realize the MOF-on-MOF heterostructure, we have employed the optimized syntheses conditions. After deposition of the bottom layer MOF, substrates are thoroughly washed before drop casting the top layer. The MOF-on-MOF geometry and the respective out-of-plane XRD patterns are shown in Fig. 3 and b. The isostructural MOFs can grow in an epitaxial manner,[17,51,67] as can be seen from the XRD patterns. In the case of UiO-66 and UiO-66-NH_2 bottom layers, the top layers also maintain the exclusive [111] orientation. This is because of very high CPO values of UiO-66 and UiO-66-NH_2. While in the case of UiO-66-Br_2, having a lower CPO value, the diffraction peak corresponding to the (200) plane of the top layer is evident, suggesting a decrease in the preferred orientation. These observations confirm that MOF-on-MOF deposition is epitaxial, and hence, in a step-by-step method, more complex heterostructures can be explored. We have further confirmed the homogeneity and stability of the MOF-on-MOF thin films from SEM images, as shown in for UiO-$66_{(B)}$-UiO-66-$Br_{2(T)}$ and IRRAS spectra (Fig. S24 and 25†).

To further validate the spatial position of the MOFs in the heterostructure, we have carried out IRRAS and X-ray

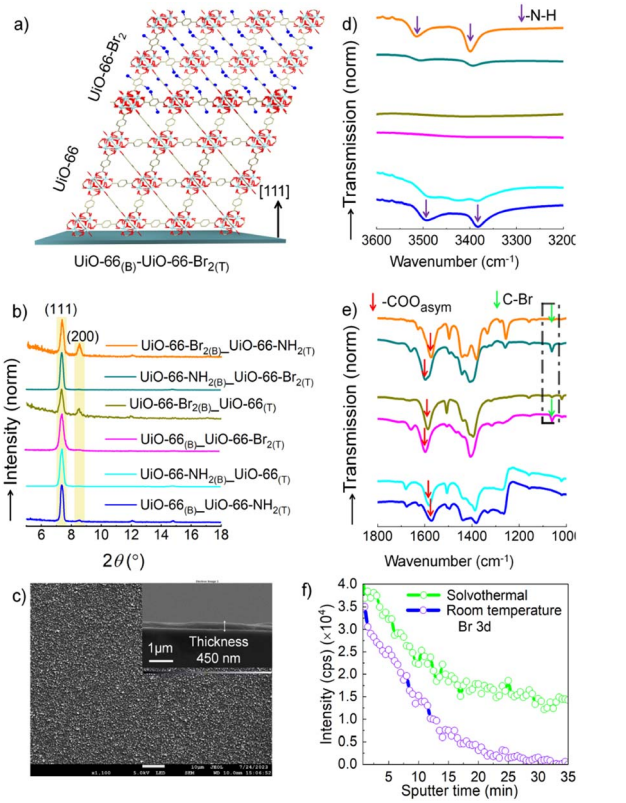

Fig. 3 a) Illustration of a MOF-on-MOF geometry for UiO-$66_{(B)}$-UiO-66-$Br_{2(T)}$, (b) out-of-plane XRD patterns of the heterostructures, (c) SEM morphology and cross-section images of UiO-$66_{(B)}$-UiO-66-$Br_{2(T)}$, (d and e) IRRAS spectra of the heterostructures showing the specific intensity changes for –N–H, –C–Br and asymmetric –COO vibrations, and (f) –Br (3d) signal at different sputtering times for UiO-$66_{(B)}$-UiO-66-$Br_{2(T)}$ and UiO-$66_{(B)}$-UiO-66-$Br_{2(T)/solvo}$.

photoelectron spectroscopy (XPS) depth profile analyses for the heterostructures. In the reflection mode IR absorption experiments, the chemical functionalities present at the thin film surface exhibit stronger absorption than those present closer to the substrate surface. Hence, IRRAS analyses help to identify the chemical groups present at the top layer of the MOF-on-MOF heterostructure.[68] The top MOF layers of the 6 different heterostructures could be easily identified by using the characteristic –COO_{asym}, –C–Br and –NH stretching frequencies. These specific frequencies are shown with an arrow in . In the case of UiO-$66_{(B)}$-UiO-66-$NH_{2(T)}$, characteristic –COO_{asym} at 1575 cm^{-1} and –NH at 3495 and 3382 cm^{-1} are evident, while for the opposite geometry –COO_{asym} at 1585 cm^{-1} corresponds to the UiO-66 MOF, and the –NH stretching frequency intensity decreases. Similar characteristic changes are also observed for the other heterostructures, confirming the formation of an epitaxial MOF-on-MOF geometry.

We have also confirmed the functional geometry of the heterostructure, UiO-$66_{(B)}$-UiO-66-$Br_{2(T)}$, by performing a depth profile analysis of the –Br(3d) signal by XPS. To evidence the advantage of the ambient condition synthesis of the heterostructure, we have also compared the depth profile analysis of a thin film, UiO-$66_{(B)}$-UiO-66-$Br_{2(T)/solvo}$, for which the top layer was deposited at high temperature (see the Experimental section). It is observed that with increasing sputtering time, the –Br signal decays rapidly for UiO-$66_{(B)}$-UiO-66-$Br_{2(T)}$, while for UiO-$66_{(B)}$-UiO-66-$Br_{2(T)/solvo}$ the Br signal did not decay much. This indicates that at higher temperature, top MOF layer precursors can diffuse into the bottom layer MOF, and *via* the linker-exchange mechanism a mixed-linker MOF is created, instead of a MOF-on-MOF geometry.

1 and 2-propanol diffusion selectivity

To validate the anisotropic distribution of the functionalities in the heterostructures, we have tested the diffusion rate of two chemical isomers in UiO-$66_{(B)}$-UiO-66-$Br_{2(T)}$ and UiO-66-$Br_{2(B)}$-UiO-$66_{(T)}$, using the QCM technique (*vide supra*). Note that the accessible pores in UiO-66 and UiO-66-Br_2 are sterically and electronically distinct. 1 and 2-propanol have a very similar kinetic diameter (~4.7–4.9 Å),[66] but have different geometries. As the pore window size of the UiO-66 MOFs is larger (~6 Å), both of the isomers can diffuse into the MOF thin films. The normalized vapour uptake rate profiles, shown in Fig. 4, indicated that 1-propanol diffuses faster in both of the heterostructure geometries (diffusivity, D ~1.4×10^{-16} and 1.7×10^{-16} m^2 s^{-1} for UiO-$66_{(B)}$-UiO-66-$Br_{2(T)}$ and UiO-66-$Br_{2(B)}$-UiO-$66_{(T)}$, respectively). 2-propanol exhibited more prominent heterostructure geometry dependent diffusivity, D ~3.3×10^{-17} and 4.8×10^{-17} m^2 s^{-1} for UiO-$66_{(B)}$-UiO-66-$Br_{2(T)}$ and UiO-66-$Br_{2(B)}$-UiO-$66_{(T)}$, respectively. Considering the mass uptake rates (*i.e.* slopes obtained from the linear fits in two different fractional uptake regions, shown with a solid line in Fig. 4), the 1 *vs.* 2-propanol selectivity values are ~2 and 1.8 for UiO-$66_{(B)}$-UiO-66-$Br_{2(T)}$ and UiO-66-$Br_{2(B)}$-UiO-$66_{(T)}$, respectively. This difference in the diffusivity can be attributed to the nature of the top-layer MOF (as diffusivity is calculated using the lower fractional uptake region, <0.2). For the –Br functionalized top layer (UiO-66-Br_2), 2-propanol diffuses slower due to stronger adsorbate–adsorbent interaction (2-propanol has a larger dipole moment than 1-propanol, possibly due to Br···2-propanol interaction). Thus the functional anisotropy effect is evident. Further exploration of this anisotropic functional structure can be used for membrane based gas separation.

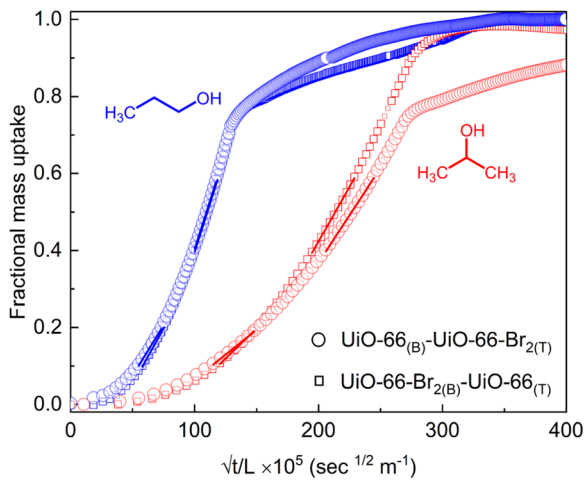

Fig. 4 Fractional mass uptake profiles of 1 and 2-propanol vapours, for two geometries of UiO-66-UiO-66-Br_2 heterostructures. The solid lines indicate linear fittings.

Conclusions

In conclusion, using a self-assembly approach of metal nodes and linkers, UiO-66 and its functionalized variant UiO-66-NH_2 and UiO-66-Br_2 MOF thin films have been synthesized under room temperature conditions. These thin films possess several notable characteristics: they exhibit highly preferential growth along the [111] direction and feature a monolithic structure with exceptional optical transparency and porosity, and have been formed under mild self-assembly conditions, allowing for step-wise, epitaxial MOF-on-MOF growth, as confirmed by XRD and IRRAS analyses. The achieved spatial distribution of the chemical functionalities in an oriented Zr-MOF thin film is unprecedented. This functional anisotropy also influences chemical isomer diffusion selectivity, as shown by 1 and 2-propanol mass uptake rate studies. The crystalline orientation and the MOF-on-MOF epitaxy represent crucial advancements in the development of novel gas separation membranes and catalytic systems. The newly established methodology paves the way for the continued exploration of intricate functionalities using the chemically resilient Zr-MOF structure, and ongoing work is dedicated to advancing these possibilities.

Data availability

The data that support the findings of this study are available from the corresponding author upon reasonable request.

Author contributions

S. P. and R. H. conceived the idea, S. P. performed the experiments and characterization, S. K. helped with SEM, P. M. carried out parts of the synthesis, and all the authors contributed to the manuscript preparation.

Conflicts of interest

There are no conflicts to declare.

Acknowledgements

We acknowledge the financial support from the Science and Engineering Research Board (SERB), Govt. of India (Project No: SRG/2022/000927) and intramural funds at TIFR Hyderabad from the Department of Atomic Energy (DAE), India, under Project Identification Number RTI 4007.

References

1 H. Furukawa, K. E. Cordova, M. O'Keeffe and O. M. Yaghi, *Science*, 2013, **341**, 1230444.
2 S. Kitagawa and R. Matsuda, *Coord. Chem. Rev.*, 2007, **251**, 2490–2509.
3 D. Yang and B. C. Gates, *ACS Catal.*, 2019, **9**, 1779–1798.
4 J. Lee, O. K. Farha, J. Roberts, K. A. Scheidt, S. T. Nguyen and J. T. Hupp, *Chem. Soc. Rev.*, 2009, **38**, 1450–1459.
5 A. Bavykina, N. Kolobov, I. S. Khan, J. A. Bau, A. Ramirez and J. Gascon, *Chem. Rev.*, 2020, **120**, 8468–8535.
6 O. K. Farha, I. Eryazici, N. C. Jeong, B. G. Hauser, C. E. Wilmer, A. A. Sarjeant, R. Q. Snurr, S. T. Nguyen, A. Ö. Yazaydın and J. T. Hupp, *J. Am. Chem. Soc.*, 2012, **134**, 15016–15021.
7 S. M. Moosavi, A. Nandy, K. M. Jablonka, D. Ongari, J. P. Janet, P. G. Boyd, Y. Lee, B. Smit and H. J. Kulik, *Nat. Commun.*, 2020, **11**, 4068.
8 A. S. Rosen, S. M. Iyer, D. Ray, Z. Yao, A. Aspuru-Guzik, L. Gagliardi, J. M. Notestein and R. Q. Snurr, *Matter*, 2021, **4**, 1578–1597.
9 M. C. So, G. P. Wiederrecht, J. E. Mondloch, J. T. Hupp and O. K. Farha, *Chem. Commun.*, 2015, **51**, 3501–3510.
10 M. G. Campbell, S. F. Liu, T. M. Swager and M. Dincă, *J. Am. Chem. Soc.*, 2015, **137**, 13780–13783.
11 W. P. Lustig, S. Mukherjee, N. D. Rudd, A. V. Desai, J. Li and S. K. Ghosh, *Chem. Soc. Rev.*, 2017, **46**, 3242–3285.
12 V. Stavila, A. A. Talin and M. D. Allendorf, *Chem. Soc. Rev.*, 2014, **43**, 5994–6010.
13 Q. Qian, P. A. Asinger, M. J. Lee, G. Han, K. Mizrahi Rodriguez, S. Lin, F. M. Benedetti, A. X. Wu, W. S. Chi and Z. P. Smith, *Chem. Rev.*, 2020, **120**, 8161–8266.
14 P. Sindhu, K. S. Ananthram, A. Jain, K. Tarafder and N. Ballav, *Nat. Commun.*, 2023, **14**, 2857.
15 Z.-Z. Ma, Q.-H. Li, Z. Wang, Z.-G. Gu and J. Zhang, *Nat. Commun.*, 2022, **13**, 6347.
16 Y.-H. Xiao, Z.-G. Gu and J. Zhang, *Nanoscale*, 2020, **12**, 12712–12730.
17 R. Haldar and C. Wöll, *Nano Res.*, 2021, **14**, 355–368.
18 S. Furukawa, J. Reboul, S. Diring, K. Sumida and S. Kitagawa, *Chem. Soc. Rev.*, 2014, **43**, 5700–5734.
19 H. Deng, C. J. Doonan, H. Furukawa, R. B. Ferreira, J. Towne, C. B. Knobler, B. Wang and O. M. Yaghi, *Science*, 2010, **327**, 846–850.
20 C. Liu, Q. Sun, L. Lin, J. Wang, C. Zhang, C. Xia, T. Bao, J. Wan, R. Huang, J. Zou and C. Yu, *Nat. Commun.*, 2020, **11**, 4971.
21 Y. Liu, A. Hori, S. Kusaka, N. Hosono, M. Li, A. Guo, D. Du, Y. Li, W. Yang, Y. Ma and R. Matsuda, *Chem. – Asian J.*, 2019, **14**, 2072–2076.
22 Y. Bai, Y. Dou, L.-H. Xie, W. Rutledge, J.-R. Li and H.-C. Zhou, *Chem. Soc. Rev.*, 2016, **45**, 2327–2367.
23 H. Yang, F. Peng, A. N. Hong, Y. Wang, X. Bu and P. Feng, *J. Am. Chem. Soc.*, 2021, **143**, 14470–14474.
24 S. M. Towsif Abtab, D. Alezi, P. M. Bhatt, A. Shkurenko, Y. Belmabkhout, H. Aggarwal, Ł. J. Weseliński, N. Alsadun, U. Samin, M. N. Hedhili and M. Eddaoudi, *Chem*, 2018, **4**, 94–105.
25 Y. Chen, K. B. Idrees, M. R. Mian, F. A. Son, C. Zhang, X. Wang and O. K. Farha, *J. Am. Chem. Soc.*, 2023, **145**, 3055–3063.
26 X. Liu, N. K. Demir, Z. Wu and K. Li, *J. Am. Chem. Soc.*, 2015, **137**, 6999–7002.
27 S. Friebe, B. Geppert, F. Steinbach and J. Caro, *ACS Appl. Mater. Interfaces*, 2017, **9**, 12878–12885.
28 J. Yan, Y. Sun, T. Ji, Y. Liu, N. Zhang, B. Sun, S. Meng, B. H. Yin, M. Wu, H. Hu and Y. Liu, *Ind. Eng. Chem. Res.*, 2023, **62**, 5973–5983.
29 Y. Sun, J. Yan, Y. Gao, T. Ji, S. Chen, C. Wang, P. Lu, Y. Li and Y. Liu, *Angew. Chem., Int. Ed.*, 2023, **62**, e202216697.
30 C. Liu, J. Wang, J. Wan and C. Yu, *Coord. Chem. Rev.*, 2021, **432**, 213743.
31 D. H. Hong, H. S. Shim, J. Ha and H. R. Moon, *Bull. Korean Chem. Soc.*, 2021, **42**, 956–969.
32 R. K. Tonnah, M. Chai, M. Abdollahzadeh, H. Xiao, M. Mohammad, E. Hosseini, M. Zakertabrizi, D. Jarrahbashi, A. Asadi, A. Razmjou and M. Asadnia, *ACS Nano*, 2023, **17**, 12445–12457.
33 H. Zhang, A. Chen, Z. Bi, X. Wang, X. Liu, Q. Kong, W. Zhang, L. Mai and G. Hu, *ACS Nano*, 2023, **17**, 24070–24079.
34 A. Knebel, P. Wulfert-Holzmann, S. Friebe, J. Pavel, I. Strauß, A. Mundstock, F. Steinbach and J. Caro, *Chem.–Eur. J.*, 2018, **24**, 5728–5733.
35 C. R. Wade, M. Li and M. Dincă, *Angew. Chem., Int. Ed.*, 2013, **52**, 13377–13381.
36 K. AlKaabi, C. R. Wade and M. Dincă, *Chem*, 2016, **1**, 264–272.
37 M. Miyamoto, S. Kohmura, H. Iwatsuka, Y. Oumi and S. Uemiya, *CrystEngComm*, 2015, **17**, 3422–3425.
38 P. K. Verma, L. Huelsenbeck, A. W. Nichols, T. Islamoglu, H. Heinrich, C. W. Machan and G. Giri, *Chem. Mater.*, 2020, **32**, 10556–10565.
39 P. Falcaro, K. Okada, T. Hara, K. Ikigaki, Y. Tokudome, A. W. Thornton, A. J. Hill, T. Williams, C. Doonan and M. Takahashi, *Nat. Mater.*, 2017, **16**, 342–348.

40 O. Shekhah, H. Wang, S. Kowarik, F. Schreiber, M. Paulus, M. Tolan, C. Sternemann, F. Evers, D. Zacher, R. A. Fischer and C. Wöll, *J. Am. Chem. Soc.*, 2007, **129**, 15118–15119.
41 M. C. So, S. Jin, H.-J. Son, G. P. Wiederrecht, O. K. Farha and J. T. Hupp, *J. Am. Chem. Soc.*, 2013, **135**, 15698–15701.
42 I. Stassen, M. Styles, G. Grenci, H. V. Gorp, W. Vanderlinden, S. D. Feyter, P. Falcaro, D. D. Vos, P. Vereecken and R. Ameloot, *Nat. Mater.*, 2016, **15**, 304–310.
43 T. Stassin, S. Rodríguez-Hermida, B. Schrode, A. J. Cruz, F. Carraro, D. Kravchenko, V. Creemers, I. Stassen, T. Hauffman, D. De Vos, P. Falcaro, R. Resel and R. Ameloot, *Chem. Commun.*, 2019, **55**, 10056–10059.
44 M. K. S. Barr, S. Nadiri, D.-H. Chen, P. G. Weidler, S. Bochmann, H. Baumgart, J. Bachmann and E. Redel, *Chem. Mater.*, 2022, **34**, 9836–9843.
45 K. B. Lausund and O. Nilsen, *Nat. Commun.*, 2016, **7**, 13578.
46 I. Stassen, M. Styles, T. Van Assche, N. Campagnol, J. Fransaer, J. Denayer, J.-C. Tan, P. Falcaro, D. De Vos and R. Ameloot, *Chem. Mater.*, 2015, **27**, 1801–1807.
47 I. Hod, W. Bury, D. M. Karlin, P. Deria, C.-W. Kung, M. J. Katz, M. So, B. Klahr, D. Jin, Y.-W. Chung, T. W. Odom, O. K. Farha and J. T. Hupp, *Adv. Mater.*, 2014, **26**, 6295–6300.
48 E. Virmani, J. M. Rotter, A. Mähringer, T. von Zons, A. Godt, T. Bein, S. Wuttke and D. D. Medina, *J. Am. Chem. Soc.*, 2018, **140**, 4812–4819.
49 M. J. Katz, Z. J. Brown, Y. J. Colón, P. W. Siu, K. A. Scheidt, R. Q. Snurr, J. T. Hupp and O. K. Farha, *Chem. Commun.*, 2013, **49**, 9449–9451.
50 K. Ikigaki, K. Okada, Y. Tokudome, T. Toyao, P. Falcaro, C. J. Doonan and M. Takahashi, *Angew. Chem., Int. Ed.*, 2019, **58**, 6886–6890.
51 Z. Wang, J. Liu, B. Lukose, Z. Gu, P. G. Weidler, H. Gliemann, T. Heine and C. Wöll, *Nano Lett.*, 2014, **14**, 1526–1529.
52 P. Sindhu, A. Prasoon, S. Rana and N. Ballav, *J. Phys. Chem. Lett.*, 2020, **11**, 6242–6248.
53 K. Zhu, R. Fan, J. Wu, B. Wang, H. Lu, X. Zheng, T. Sun, S. Gai, X. Zhou and Y. Yang, *ACS Appl. Mater. Interfaces*, 2020, **12**, 58239–58251.
54 A. Chandresh, X. Liu, C. Wöll and L. Heinke, *Adv. Sci.*, 2021, **8**, 2001884.
55 P. Malik and R. Haldar, *Mol. Syst. Des. Eng.*, 2022, **7**, 873–877.
56 S. Biswas and P. Van Der Voort, *Eur. J. Inorg. Chem.*, 2013, **2013**, 2154–2160.
57 T. Hashem, E. P. Valadez Sánchez, P. G. Weidler, H. Gliemann, M. H. Alkordi and C. Wöll, *ChemistryOpen*, 2020, **9**, 524–527.
58 A. L. Semrau and R. A. Fischer, *Chem.–Eur. J.*, 2021, **27**, 8509–8516.
59 M. R. DeStefano, T. Islamoglu, S. J. Garibay, J. T. Hupp and O. K. Farha, *Chem. Mater.*, 2017, **29**, 1357–1361.
60 L. Valenzano, B. Civalleri, S. Chavan, S. Bordiga, M. H. Nilsen, S. Jakobsen, K. P. Lillerud and C. Lamberti, *Chem. Mater.*, 2011, **23**, 1700–1718.
61 M. Kandiah, M. H. Nilsen, S. Usseglio, S. Jakobsen, U. Olsbye, M. Tilset, C. Larabi, E. A. Quadrelli, F. Bonino and K. P. Lillerud, *Chem. Mater.*, 2010, **22**, 6632–6640.
62 L. Wei, Y. Zhang, J. Jiang, Y. Yang and H. Liu, *Langmuir*, 2023, **39**, 3678–3691.
63 R. Haldar, L. Heinke and C. Wöll, *Adv. Mater.*, 2020, **32**, 1905227.
64 C. H. Sharp, B. C. Bukowski, H. Li, E. M. Johnson, S. Ilic, A. J. Morris, D. Gersappe, R. Q. Snurr and J. R. Morris, *Chem. Soc. Rev.*, 2021, **50**, 11530–11558.
65 O. Zybaylo, O. Shekhah, H. Wang, M. Tafipolsky, R. Schmid, D. Johannsmann and C. Wöll, *Phys. Chem. Chem. Phys.*, 2010, **12**, 8093–8098.
66 J.-R. Li, R. J. Kuppler and H.-C. Zhou, *Chem. Soc. Rev.*, 2009, **38**, 1477–1504.
67 J. Ha and H. R. Moon, *CrystEngComm*, 2021, **23**, 2337–2354.
68 X.-J. Yu, Y.-M. Xian, C. Wang, H.-L. Mao, M. Kind, T. Abu-Husein, Z. Chen, S.-B. Zhu, B. Ren, A. Terfort and J.-L. Zhuang, *J. Am. Chem. Soc.*, 2019, **141**, 18984–18993.